

SPA: Efficient User-Preference Alignment against Uncertainty in Medical Image Segmentation

Jiayuan Zhu *

University of Oxford

jiayuan.zhu@eng.ox.ac.uk

Junde Wu *

University of Oxford

junde.wu@eng.ox.ac.uk

Cheng Ouyang

University of Oxford

cheng.ouyang@eng.ox.ac.uk

Konstantinos Kamnitsas

University of Oxford

konstantinos.kamnitsas@eng.ox.ac.uk

J. Alison Noble

University of Oxford

alison.noble@eng.ox.ac.uk

Abstract

Medical image segmentation data inherently contain uncertainty. This can stem from both imperfect image quality and variability in labeling preferences on ambiguous pixels, which depend on annotator expertise and the clinical context of the annotations. For instance, a boundary pixel might be labeled as tumor in diagnosis to avoid under-estimation of severity, but as normal tissue in radiotherapy to prevent damage to sensitive structures. As segmentation preferences vary across downstream applications, it is often desirable for an image segmentation model to offer user-adaptable predictions rather than a fixed output. While prior uncertainty-aware and interactive methods offer adaptability, they are inefficient at test time: uncertainty-aware models require users to choose from numerous similar outputs, while interactive models demand significant user input through click or box prompts to refine segmentation. To address these challenges, we propose **SPA**, a new Segmentation Preference Alignment framework that efficiently adapts to diverse test-time preferences with minimal human interaction. By presenting users with a select few, distinct segmentation candidates that best capture uncertainties, it reduces the user workload to reach the preferred segmentation. To accommodate user preference, we introduce a probabilistic mechanism that leverages user feedback to adapt a model’s segmentation preference. The proposed framework is evaluated on several medical image segmentation tasks: color fundus images, lung lesion and kidney CT scans, MRI scans of brain and prostate. SPA shows 1) a significant reduction in user time and effort compared to existing interactive segmentation approaches, 2) strong adaptability based on human feedback, and 3) state-of-the-art image segmentation performance across different

imaging modalities and semantic labels.

1. Introduction

Deep learning-based medical image segmentation has achieved remarkable progress over the past decade [5, 26, 30]. However, existing approaches often fail when applied to real-world clinical scenarios. A critical challenge is how to handle the inherent uncertainties in medical images [12]. A single medical image may have multiple different valid segmentation results, depending on the labeling criteria for a specific medical context. For example, in glioma detection from brain CT scans, it is often preferred to include surrounding tissue rather than risk missing part of the tumor [2]. In contrast, in radiation therapy for low-grade glioma, undersegmentation is preferred to protect sensitive brain tissue from excessive radiation damage [25]. Therefore, it is essential to develop adaptive methodologies that align segmentation uncertainties with specific labeling preferences for different clinical needs.

Existing uncertainty-aware approaches [3, 16, 21, 27] represent segmentation uncertainty to users by generating numerous stochastic predictions (Fig. 1 (a)). However, users often have to carefully choose from countless similar-looking candidates, making the process time-consuming. Furthermore, since these models cannot incorporate human feedback for adjustments, there is a risk that none of the predictions be satisfying.

Incorporating human feedback into segmentation, often in the form of visual prompts (such as clicks and bounding boxes) has shown promise [6, 17, 23, 29]. However, most such interactive segmentation approaches do not incorporate uncertainty. Additionally, existing visual prompts are often cumbersome to attain in the real world, as they require pixel-level interaction input from a user (Fig. 1 (b)).

*equal contribution

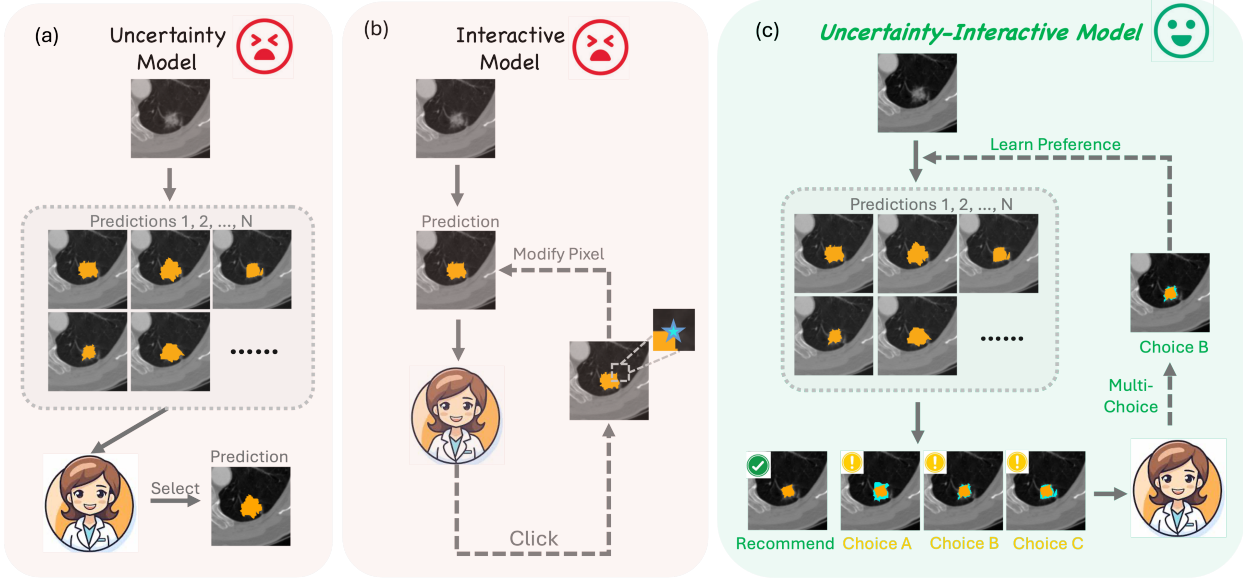


Figure 1. (a) Existing uncertainty-aware models require users to choose from numerous similar-looking candidates, making the process labor-intensive and time-consuming. (b) Interactive segmentation models lack the ability to incorporate image uncertainty and rely heavily on pixel-level user inputs, which require a substantial amount of time and effort. (c) Our uncertainty-aware interactive segmentation model, SPA, efficiently achieves segmentations whose decisions on uncertain pixels are aligned with users preferences. This is achieved by modeling uncertainties and human interactions. At inference time, users are presented with one recommended prediction and a few representative segmentations that capture uncertainty, allowing users to select the one best aligned with their clinical needs. If the user is unsatisfied with the recommended prediction, the model learns from the users' selections, adapts itself, and presents users a new set of representative segmentations. Our approach minimizes user interactions and eliminates the need for painstaking pixel-wise adjustments compared to conventional interactive segmentation models.

To address the above challenges, we propose to present users a small number of distinct segmentations to represent uncertainty. It allows users to select their preferred option, simplifying interactive refinement into a straightforward multiple-choice selection. In this paper, we introduce **SPA**, a new approach for efficient Segmentation Preference Alignment with uncertainty in medical image segmentation (Fig. 1). SPA presents image uncertainties by generating multiple segmentations. Instead of providing users with numerous similar-looking predictions as in conventional uncertainty-aware segmentations, our model offers one recommended prediction and four representative segmentation candidates per iteration. Once the user selects an option, SPA rapidly adapts through iterative refinement, aligning efficiently with the user's segmentation preference in only a few iterations. Our experiment demonstrates that a user can segment 35% more images with 39% fewer iterations compared to previous interactive models. This highlights SPA's potential for real-world clinical applications. In summary, our contributions are:

- We introduce SPA, a new segmentation framework that can align to users' decision preferences toward ambiguous/uncertain pixels at inference time. Such preferences often vary with clinical contexts, which existing segmentation models cannot adapt to efficiently.

- We propose to model uncertainties in pixel-wise predictions under diverse preferences as a parameterized latent distribution. This modeling enables rapid adaptation to user preferences with minimal iterations at inference time.
- We develop a multi-choice interaction mechanism to receive user preferences at inference time, providing a more friendly and effortless user experience than existing works.
- We compare SPA with deterministic, uncertainty-aware, and interactive SOTA methods. SPA achieves superior results measured by Dice Score for three multi-clinician annotated datasets (REFUGE2, LIDC-IDRI and QUBIQ). SPA also consistently outperforms interactive methods in terms of requiring fewer rounds of user interactions.

2. Related Work

Uncertainty-aware Medical Segmentation Uncertainty in medical images cannot be reduced by adding more data or using more complex models [18]. Techniques such as model ensembling, label sampling [14], and multi-head strategies [10] attempt to address this uncertainty by generating a range of potential predictions that reflect different user preferences [13, 35]. Probabilistic segmentation methods, including ProbUNet [19], PhiSeg [3], CM-Net [33] and MRNet [15] explicitly model the posterior distribution of parameters

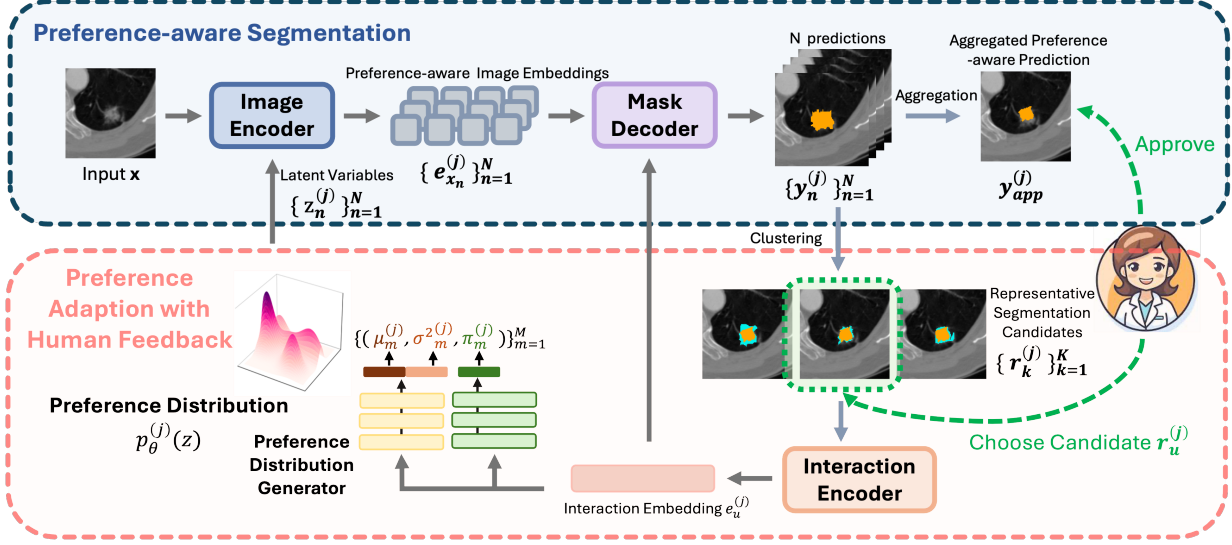


Figure 2. Overall framework of SPA. The inference process comprises of two steps: *Preference-aware Segmentation* and *Preference Adaptation with Human Feedback*. At iteration j , SPA takes the input image \mathbf{x} , an interaction embedding $e_u^{(j)}$, and latent variables $\{\mathbf{z}_n^{(j)}\}_{n=1}^N$ drawn from the preference distribution $p_\theta^{(j)}(z)$ to generate N segmentation predictions. These predictions are then combined into an aggregated preference-aware prediction $\mathbf{y}_{app}^{(j)}$. If the user is not satisfied with $\mathbf{y}_{app}^{(j)}$, SPA generates K representative segmentation candidates $\{\mathbf{r}_k^{(j)}\}_{k=1}^K$ in the adaptation step. The user selects the preferred segmentation candidate $\mathbf{r}_u^{(j)}$. The preference distribution is then updated to $p_\theta^{(j+1)}(z)$ based on this choice. This process iterates until the segmentation meets clinical satisfaction.

or predictions to capture uncertainty. However, these approaches often generate multiple predictions, requiring users to review each individually. Moreover, the predictions may not perfectly match the specific clinical context, and some techniques rely on prior knowledge of the expertise of a clinician, complicating adoption into clinical practice. In contrast, a more efficient approach is to incorporate human interactions, allowing users to refine segmentations through direct interaction to better align with the clinical context.

Interactive Medical Segmentation Interactive segmentation is an iterative process where automated segmentation results are refined through user input until they reach a desired output. Previous methods [17, 28, 31] have modified predictions based on user interaction at the pixel level, with some achieving success in the medical domain [8, 24, 32, 34]. However, these interactive models often do not address the inherent uncertainty in medical images. Additionally, they may require numerous iterations to align with the user preference for a specific clinical context, given the existence of multiple valid segmentations. An interactive model capable of incorporating image uncertainties and learning from user interactions would reduce the number of iterations required to achieve a desired result.

3. Methodology

3.1. Model user preferences as latent distributions

We assume that each user’s decisions on uncertain/ambiguous pixels, based on their preference and

stemming from different medical contexts, can be modeled as *i.i.d.* samples drawn from a parameterized distribution. To represent this user preferences for different clinical contexts, we model this *preference distribution* $p_\theta(z)$ as a mixture of M Gaussian distributions:

$$p_\theta(z) = \sum_{m=1}^M \pi_m \mathcal{N}(z | \mu_m, \sigma_m^2) \quad (1)$$

where $\mathcal{N}(z | \mu_m, \sigma_m^2)$ denotes the Gaussian component for user m , with mean μ_m and variance σ_m^2 . The mixture weights π_m satisfy $\pi_m > 0$ and $\sum_{m=1}^M \pi_m = 1$. Each component in this mixture model reflects a specific user segmentation preference, enabling the framework to generate segmentation predictions that capture discrepancies across users. In our segmentation framework, $z \sim p_\theta(z)$ is implemented as a conditioning signal injected into a neural network, predicated the subtle preference-dependent variability in segmentation outputs.

Modeling user preferences as parameterized distributions is highly adaptable, as the distribution $p_\theta(z)$ can be iteratively updated via maximum likelihood based on new observations of user interactions at inference time ¹.

We integrate the preference distribution $p_\theta(z)$ into the segmentation workflow, as follows. In each iteration, we sample latent variables $\{\mathbf{z}_n\}_{n=1}^N$ from $p_\theta(z)$ to capture vari-

¹We provide a theoretical proof in the appendix to demonstrate that, given sufficient interactions from a specific user u , the preference distribution $p_\theta(z)$ will converge to the user’s personalized distribution $\mathcal{N}(\mu_u, \sigma_u^2)$.

ations under user preferences ². During training, the model learns $p_\theta(z)$ through user feedback simulated from annotated segmentations from multiple users. At inference, the model can efficiently adapt to user preferences by estimating the maximum likelihood based on the feedback of a user.

3.2. Overall Workflow

We propose SPA, which learns to model human preferences by preference distribution $p_\theta(z)$ during training, enabling it to efficiently model new user preferences at inference through interaction. Our framework also simplifies and improves the robustness of interaction by replacing pixel-level clicking with multi-choice selection.

Formally, our goal is to learn a general function $f(\cdot, \cdot)$ that can adapt to different user preferences u 's through an interaction process: $\mathbf{y} = f(\mathbf{x}, \mathbf{r}_u)$, where $\mathbf{x} \in \mathbb{R}^{H \times W \times C}$ is the input image, and \mathbf{r}_u reflects human interaction. The training details are provided in Section 3.5 and Algorithm 1.

Specifically, our SPA framework consists of two main modules (Fig. 2): *Preference-aware Segmentation* (Section 3.3) and *Preference Adaption with Human Feedback* (Section 3.4). Our *Preference-aware Segmentation* generates multiple valid segmentations to represent image uncertainty (oftentimes *aleatoric*) and the *Preference Adaption with Human Feedback* aligns these segmentations iteratively with specific user preferences.

In inference, as shown in the upper part of Fig. 2, given a raw image \mathbf{x} , *Preference-aware Segmentation* generates N segmentation predictions $\{\mathbf{y}_n^{(j)}\}_{n=1}^N$, conditioned by the interaction embedding $e_u^{(j)}$ representing the user selection, and latent variables $\{\mathbf{z}_n^{(j)}\}_{n=1}^N$ sampled from the preference distribution $p_\theta^{(j)}(z)$ at iteration j . We use the user's first point prompt to produce e_u^0 and $p_\theta^0(z)$ for the initialization. Predictions $\{\mathbf{y}_n^{(j)}\}_{n=1}^N$ reflect uncertainty from individual subtle preferences, which is controlled by $\mathbf{z}_n^{(j)}$. These predictions are combined into one aggregated preference-aware prediction $\mathbf{y}_{app}^{(j)}$ and K Representative Segmentation Candidates $\{\mathbf{r}_k^{(j)}\}_{k=1}^K$. If the user approves $\mathbf{y}_{app}^{(j)}$, it will be used as the final segmentation and the iteration ends. Otherwise, the framework uses the *Preference Adaption with Human Feedback* step for further refinement, as shown in the lower part of Fig. 2: The user then selects the segmentation $\mathbf{r}_u^{(j)}$ that best aligns with their preference. The preference distribution $p_\theta^{(j)}(z)$ is further updated to $p_\theta^{(j+1)}(z)$ based on this feedback. This iterative process continues until the user is satisfied with the segmentation.

²Preliminary experiments with MRNet [15] given in the appendix suggest that while segmentation performance varies between users, each user demonstrates consistent results. These observations indicate that modeling interaction behavior can effectively learn user preferences, thereby improving modeling efficiency.

3.3. Preference-aware Segmentation

As shown in the upper part of Fig. 2, our *Preference-aware Segmentation* step involves an image encoder and a mask decoder. Given an input image $\mathbf{x} \in \mathbb{R}^{H \times W \times C}$, we first obtain a general image embedding $\mathbf{e}_x^{(j)} \in \mathbb{R}^{L \times \frac{H}{P} \times \frac{W}{P}}$ for iteration j , where L represents the output channels and P is the Vision Transformer (ViT) patch size. This embedding is generated using a pre-trained ViT [11]. Additionally, we sample N preference conditions $\{\mathbf{z}_n^{(j)}\}_{n=1}^N$ from the preference distribution $p_\theta^{(j)}(z)$. Each $\mathbf{z}_n^{(j)} \in \mathbb{R}^{L \times \frac{H}{P} \times \frac{W}{P}}$ is concatenated with the general image embedding $\mathbf{e}_x^{(j)}$, and then processed through three convolutional layers and ReLU activations to produce a set of preference-aware image embeddings $\{\mathbf{e}_{x_n}^{(j)}\}_{n=1}^N$, where each $\mathbf{e}_{x_n}^{(j)} \in \mathbb{R}^{L \times \frac{H}{P} \times \frac{W}{P}}$.

We then employ a mask decoder to predict segmentation masks $\{\mathbf{y}_n^{(j)}\}_{n=1}^N$ from $\{\mathbf{e}_{x_n}^{(j)}\}_{n=1}^N$ and the interaction embedding $e_u^{(j)}$ (Section 3.4). The decoder follows the same architecture as SAM [17]. The final preference-aware prediction is aggregated as $\mathbf{y}_{app}^{(j)} = \mathbb{1}_{0.5} \left(\frac{1}{N} \sum_{n=1}^N \mathbf{y}_n^{(j)} \right)$.

3.4. Preference Adaption with Human Feedback

Receiving user's choice as preference. Beyond $\mathbf{y}_{app}^{(j)}$, our model also provides K Representative Segmentation Candidates $\{\mathbf{r}_k^{(j)}\}_{k=1}^K$ for further selection, as shown in the lower part of Fig. 2. These candidates reflect distinct possible ways to adapt the prediction. To create $\{\mathbf{r}_k^{(j)}\}_{k=1}^K$, K-means clustering is applied to the predictions $\{\mathbf{y}_n^{(j)}\}_{n=1}^N$. Each cluster produces a representative segmentation candidate $\mathbf{r}_k^{(j)} \in \{\mathbf{r}_k^{(j)}\}_{k=1}^K$ as the centroid of the cluster. We then highlight the pixel-wise differences $\{\Delta_{\mathbf{r}_k}^{(j)}\}_{k=1}^K$ between $\mathbf{y}_{app}^{(j)}$ and $\mathbf{r}_k^{(j)}$ to the users. The positive and negative differences are represented in different colors for the convenience of selection. The users then pick their preferred $\Delta_{\mathbf{r}_u}^{(j)}$, which determines the corresponding representative segmentation candidate $\mathbf{r}_u^{(j)}$. The $\mathbf{r}_u^{(j)}$ is then sent into the interaction encoder mapping into a L -dimensional feedback embedding e_u (Fig. 2). We use SAM prompt encoder, including its point and mask branches, as our interaction encoder, allowing it to accept both point and mask inputs.

Updating preference distribution. Given the interaction embedding $e_u^{(j)}$, the preference distribution $p_\theta^{(j)}(z)$ will be updated to $p_\theta^{(j+1)}(z)$ with parameters $\theta = \{(\mu_m^{(j+1)}, \sigma_m^{(j+1)}, \pi_m^{(j+1)})\}_{m=1}^M$. Specifically, since obtaining ground-truth embedding samples directly from a given mask is challenging, we replace the analytically updated GMMs with a neural network-based predictor, that we call the Preference Distribution Generator. It adaptively constructs GMMs by predicting their parameters θ based on human feedback $e_u^{(j)}$. This approach employs amortized inference to efficiently estimate GMM parameters. Given $e_u^{(j)}$, we use six forward layers to jointly predict $\mu_m^{(j)}$ and

Algorithm 1: SPA Training Process

```

Input: Image  $\mathbf{x}$ , user-preferred representative
segmentation candidate  $\mathbf{r}_u$ 
Output: Preference-aware Segmentation  $\mathbf{y}_{app}$ 
/* Definitions */
Preference Distribution Generator:  $E_{\theta_{\mu_m; \sigma_m; \pi_m}}(\cdot)$ 
generating  $\{(\mu_m, \sigma_m^2, \pi_m)\}_{m=1}^M$  to construct  $p_\theta$ ;
Interaction Encoder:  $E_I(\cdot)$ ; Number of samples:  $N$ ;
Number of representative segmentation candidates:
 $K$ ;
Function GenMask( $\mathbf{e}_x, p_\theta, e_u$ ):
    Sample  $n$  embeddings:  $\mathbf{z}_n \sim p_\theta$ , then
         $\mathbf{e}_{x_n} = \text{ReLU}(\text{Conv}(\mathbf{e}_x \oplus \mathbf{z}_n))$ ;
         $\mathbf{y}_n = \text{Decoder}(\mathbf{e}_{x_n}, e_u)$ ;
         $\mathbf{y}_{app} = \mathbb{1}_{0.5} \left( \frac{1}{N} \sum_{n=1}^N \mathbf{y}_n \right)$ ;
    return  $\mathbf{y}_{app}, \{\mathbf{y}_n\}_{n=1}^N$ ;
/* Training Loop */
for  $t = 1$  to  $MAX\_TRAINING\_UPDATES$  do
    Initialize  $\mathbf{y}, p_\theta, \mathbf{r}_u$  as described in Section 3.2
    for  $j = 1$  to  $MAX\_USER\_ITERATIONS$  do
        Extract:  $\mathbf{e}_x = \text{ViT}(\mathbf{x}), e_u = E_I(\mathbf{r}_u)$ ;
        Call  $\mathbf{y}_{app, -}^{ori} = \text{GenMask}(\mathbf{e}_x, p_\theta, e_u)$ ;
        /* Update Preference
        Distribution Generator */
        Update mean and variance:  $\theta'_{\mu_m; \sigma_m} =$ 
             $\theta_{\mu_m; \sigma_m} + \alpha \nabla_{\theta_{\mu_m; \sigma_m}} \mathcal{L}_{CE}(\mathbf{y}_{app}^{ori}, \mathbf{y})$ ;
        Compute GMM responsibilities (E-step):
             $\pi_m^{gt} = \frac{\pi_m p(y|\mu_m, \sigma_m^2)}{\sum_{m=1}^M \pi_m p(y|\mu_m, \sigma_m^2)}$ ;
        Update GMM weights:
             $\theta'_{\pi_m} = \theta_{\pi_m} + \alpha \nabla_{\theta_{\pi_m}} \mathcal{L}_{MSE}(\pi_m^{gt}, \pi_m)$ ;
        Call  $\mathbf{y}_{app, -}^{gmm} =$ 
             $\text{GenMask}(\mathbf{e}_x, p_\theta(\theta'_{\mu_m; \sigma_m}; \theta'_{\pi_m}), e_u)$ ;
        /* Segmentation Update */
        Update segmentation and interaction
        encoders:
             $\theta'_{PSeg} = \theta_{PSeg} + \alpha \nabla_{\theta_{PSeg}} \mathcal{L}_{CE}(\mathbf{y}_{app}^{gmm}, \mathbf{y})$ ,
             $\theta'_{EI} = \theta_{EI} + \alpha \nabla_{\theta_{EI}} \mathcal{L}_{CE}(\mathbf{y}_{app}^{gmm}, \mathbf{y})$ ;
        Call  $\mathbf{y}_{app}^{fin}, \{\mathbf{y}_n^{fin}\}_{n=1}^N =$ 
             $\text{GenMask}(\mathbf{e}_x, p_\theta(\theta'_{\mu_m; \sigma_m}; \theta'_{\pi_m}), e'_u)$ ;
        /* Simulate User Selection for
        the Next Iteration */
        Get  $K$  Representative Candidates:
             $\{\mathbf{r}_k\}_{k=1}^K = \text{KMeans}(\{\mathbf{y}_n^{fin}\}_{n=1}^N)$ ;
        Select preferred representative candidate:
             $\mathbf{r}_u = \arg \min_{\mathbf{r}_k} \|\mathbf{r}_k - \mathbf{y}_{app}^{fin}\|_2$ ;

```

$\sigma_m^{(j)}$ from a $2m$ -length vector, and use another six forward layers to predict $\pi_m^{(j)}$ (Fig. 2 lower part). The predictor of

$\mu_m^{(j)}$ and $\sigma_m^{(j)}$ is updated by the backpropagation from the final supervision y , while the predictor of $\pi_m^{(j)}$ is separately updated by the supervision from ground-truth $\pi_m^{GT(j)}$, since given $\mu_m^{(j)}, \sigma_m^{(j)}$, and \mathbf{y} , we can get the analytical solution for $\pi_m^{(j)}$ from the GMM E-step (Algorithm 1).

Segmentations with iteratively aligned preference. In the next iteration, new latent variables $\{\mathbf{z}_n^{(j+1)}\}_{n=1}^N$ are sampled from the updated preference distribution $p_\theta^{(j+1)}(z)$ and undergo *Preference-aware Segmentation* together with the input image \mathbf{x} and interaction embedding $e_u^{(j)}$.

Inference across input images. For each input image \mathbf{x} , r_u is initialized as a user point prompt (similar to SAM), and an initial $p_\theta(z)$ is predicted based on r_u .

3.5. Training Details

In training, for each \mathbf{x} , we initialize the ground truth \mathbf{y} as a stochastic combination of collected multi-rater labels: $\mathbf{y} = \mathbb{1}_{0.5} (\sum A \times Y)$, where A represents the weights uniformly sampled from $[0, 1]$ and Y denotes the set of user annotations. We then simulate user interaction and iteratively update the distribution generator to produce $p_\theta^{(j)}(z)$ from r_u , and the segmentation model to predict $\{\mathbf{y}_n^{(j)}\}_{n=1}^N$ based on $p_\theta^{(j)}(z)$. The initial \mathbf{r}_u is simulated by randomly selecting a point from the ground truth. Supervision is then applied to ensure that the final jointly produced aggregation $\mathbf{y}_{app}^{(j)}$ matches ground truth \mathbf{y} . The full training pipeline is in Algorithm 1.

4. Experiment

We conducted experiments to validate the effectiveness of SPA across seven uncertainty segmentation tasks represented by multi-clinician, using data from three medical imaging modalities: color fundus images, lung lesion and kidney CT scans, brain and prostate MRI scans. SPA consistently achieves SOTA performance compared to deterministic, uncertainty-aware, and interactive models. Notably, SPA outperforms interactive models with significantly fewer iterations and it demonstrates strong generalization on unseen users. Human evaluation further shows that SPA requires less time and fewer interactions to meet human expectations. Our results also show that predictions increasingly align with selected users while diverging from those excluded. Ablation studies highlight the necessity of each component for optimal segmentation. Additional analysis of representative segmentation candidates' similarities across iterations and prediction changes after each interaction are detailed in the appendix.

4.1. Dataset

REFUGE2 benchmark [9] is a publicly available fundus image dataset for glaucoma analysis, including optic cup segmentation. REFUGE2 includes annotations from seven

Table 1. SPA Outperforms the SOTA in Dice Score (%). We compared deterministic, uncertainty-aware, and interactive models with Dice Score as the metric. SAM-series models use clicks for interaction, while SAM-U uses bounding boxes. SPA, with its multi-choice representative segmentation candidate mechanism, consistently outperforms the other models for the seven tasks. 1-Iter and 3-Iter indicate performance after one and three iterations, respectively.

| Methods | Category | 1-Iter | 3-Iter | REFUGE2 | LIDC | BrainTumor | Prostate1 | Prostate2 | BrainGrowth | Kidney | Ave |
|---------------|----------|--------|--------|--------------|--------------|--------------|--------------|--------------|--------------|--------------|--------------|
| UNet | Det | ✓ | | 68.94 | 62.99 | 87.30 | 83.89 | 77.22 | 62.02 | 82.40 | 74.96 |
| TransUNet | | ✓ | | 80.83 | 64.09 | 90.14 | 83.35 | 68.34 | 86.58 | 52.99 | 75.19 |
| SwinUNet | | ✓ | | 78.67 | 59.45 | 91.23 | 82.02 | 74.19 | 74.88 | 69.41 | 75.69 |
| Ensemble UNet | Unc | ✓ | | 70.75 | 63.84 | 90.56 | 85.27 | 79.07 | 71.69 | 89.30 | 78.64 |
| ProbUNet | | ✓ | | 68.93 | 48.52 | 89.02 | 72.13 | 66.84 | 75.59 | 75.73 | 70.96 |
| LS-Unet | | ✓ | | 73.32 | 62.05 | 90.89 | 87.92 | 81.59 | 85.63 | 72.31 | 79.10 |
| MH-Unet | | ✓ | | 72.33 | 62.60 | 86.74 | 87.03 | 75.61 | 83.54 | 73.44 | 77.32 |
| MRNet | | ✓ | | 80.56 | 63.29 | 85.84 | 87.55 | 70.82 | 84.41 | 61.30 | 76.25 |
| SAM | Int | ✓ | | 82.59 | 66.68 | 91.55 | 92.82 | 77.04 | 86.63 | 85.72 | 83.29 |
| MedSAM | | ✓ | | 82.34 | 68.42 | 92.67 | 89.69 | 74.70 | 85.91 | 78.02 | 81.68 |
| MSA | | ✓ | | 83.03 | 66.88 | 88.16 | 89.06 | 68.94 | 80.62 | 25.29 | 71.71 |
| SAM-U V1 | Unc-Int | ✓ | | 82.45 | 62.24 | 92.67 | 81.46 | 66.56 | 87.79 | 89.50 | 80.38 |
| SAM-U V2 | | ✓ | | 80.66 | 64.82 | 93.11 | 91.89 | 72.91 | 87.51 | 90.74 | 83.09 |
| SPA | | ✓ | | 83.47 | 88.07 | 94.29 | 93.12 | 83.34 | 88.14 | 94.08 | 89.22 |
| SAM | Int | | ✓ | 82.61 | 66.71 | 92.14 | 92.72 | 77.54 | 86.58 | 90.43 | 84.10 |
| MedSAM | | | ✓ | 82.13 | 68.45 | 93.26 | 90.05 | 73.81 | 86.09 | 79.88 | 81.95 |
| MSA | | | ✓ | 83.08 | 66.87 | 91.25 | 90.22 | 71.34 | 81.87 | 46.76 | 75.91 |
| SAM-U V1 | Unc-Int | | ✓ | 82.10 | 62.84 | 92.31 | 81.79 | 66.74 | 87.84 | 89.24 | 80.40 |
| SAM-U V2 | | | ✓ | 80.54 | 65.44 | 92.40 | 90.00 | 73.17 | 87.87 | 91.35 | 82.96 |
| SPA | | | ✓ | 85.42 | 88.56 | 94.31 | 92.97 | 84.05 | 88.18 | 94.26 | 89.68 |

ophthalmologists, each with an average of eight years of experience. It contains 400 training and 400 test images.

LIDC-IDRI benchmark [1, 7] originally consisted of 3D lung CT scans with semantic segmentations of possible lung abnormalities, annotated by four radiologists. We use a pre-processed version from [20] of 15,096 2D CT images. After an 80-20 train-test split, the training and test datasets contain 12,077 and 3,019 images, respectively.

QUBIQ benchmark [22] consists of one MRI brain tumor task (three annotations, 28 training cases, 4 testing cases); two MRI prostate tasks (six annotations, 48 training cases, 7 testing cases); one MRI brain-growth task (seven annotations, 34 training cases, 5 testing cases); and one CT kidney task (three annotations, 20 training cases, 4 testing cases).

4.2. Implementation Details

Our network was implemented using PyTorch v1.12 and trained/tested on an RTX A4000 with 16GB of memory. During training, we used the Adam optimizer with an initial learning rate of $1e^{-4}$ and adjusted it using StepLR strategy. $L = 256$ features were extracted to generate feature embeddings and $N = 48$ latent variables were sampled from the preference distribution $p_\theta^{(j)}(z)$, which was modeled with $M = 16$ Gaussian components. We generated $K = 4$ representative segmentation candidates to allow multi-choice selection and set $MAX_USER_ITERATIONS$ to 6. It takes 0.2 second per iteration to generate the prediction and the representative segmentation candidates, acceptable for human-in-the-loop settings.

We used **SAM-ViT/B** as the segmentation backbone. Additional implementation details are provided in the appendix. Deterministic segmentation methods with multiple annotations were trained with majority vote labels. For SAM-series

interactive models, click or bounding box prompts were uniformly generated based on the original model settings.

4.3. Experimental Results

4.3.1. Performance Comparison with SOTA Methods

To demonstrate the advantages of SPA, we compared it with SOTA methods, classified into deterministic methods (UNet [26], TransUNet [5], SwinUNet [4]), uncertainty-aware methods (Ensemble UNet, ProbUNet [19], LS-Unet [14], MH-Unet [10], MRNet [15]), and interactive methods (SAM [17], MedSAM [24], MSA [32]). We also compared SPA with SAM-U [8], an uncertainty-interactive method that simply introduces uncertainty by generating multiple prompts. SAM-U was evaluated using both SAM and MedSAM backbones with bounding boxes as the interaction strategy, named SAM-U V1 and SAM-U V2, respectively. Other SAM-series methods relied on user clicks for interactions. Results for interactive models were reported after one and three iterations.

SPA consistently outperforms all methods, achieving an average Dice Score of 89.68% after three iterations. Table 1 provides a quantitative comparison using Dice Score as the metric. The improvement is particularly notable for the LIDC segmentation task, where SPA improves on current SOTA methods by 20%. Even after one iteration, SPA demonstrates superior performance relative to the other methods. Fig. 3 shows visual comparisons between SPA and other SOTA methods, presenting segmentations after six iterations for the interactive models. The results qualitatively indicate that the segmentations predicted by SPA align more closely with the ground truth, especially in the boundary regions.

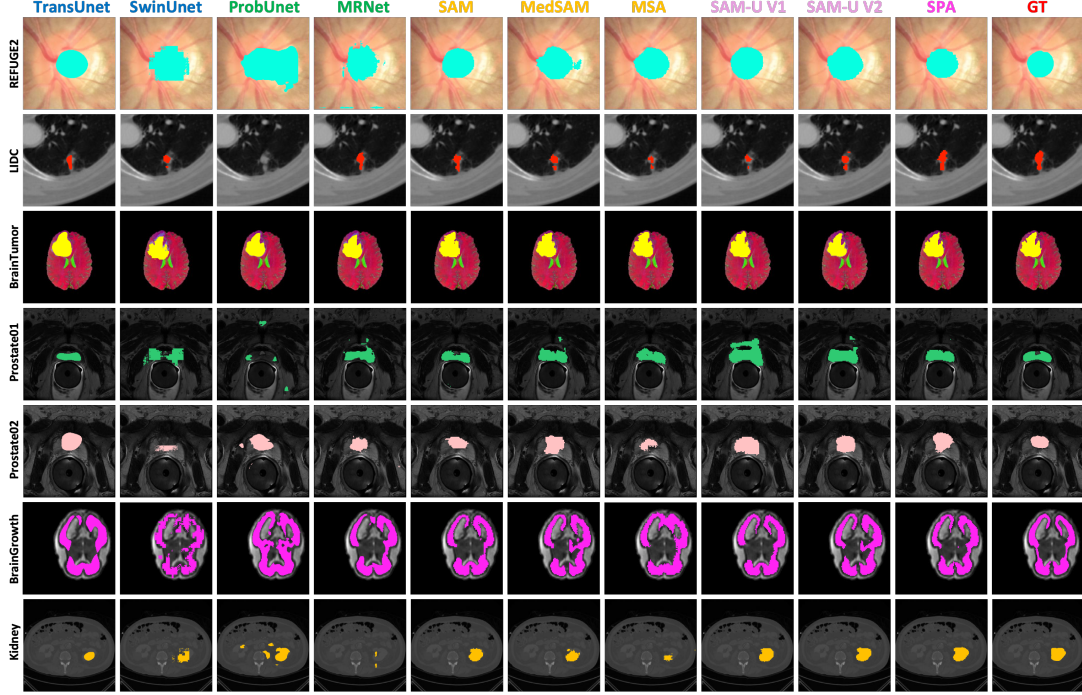


Figure 3. SPA Shows Superior Segmentation Visualization. Visual comparison of segmentation results with deterministic, uncertainty-aware, and interactive models after six iterations. SPA provides better adaptability, particularly at boundary regions.

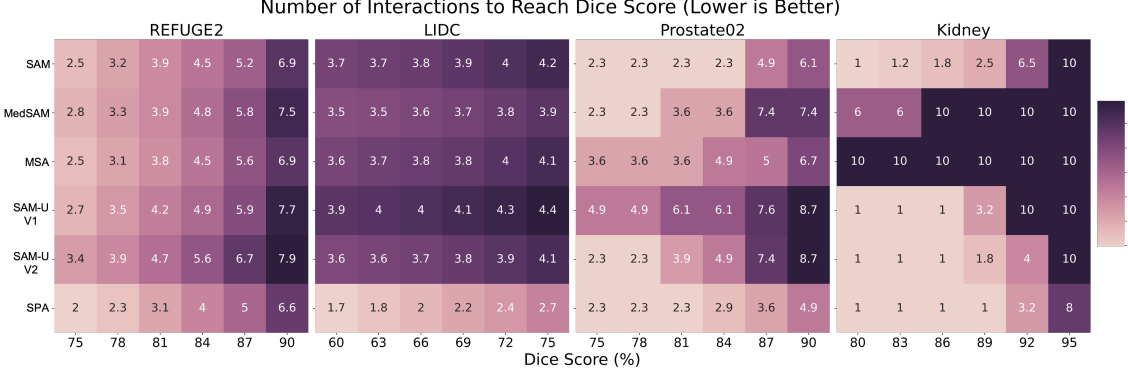


Figure 4. SPA Demonstrates Extraordinary Efficiency. Efficiency analysis comparing the average number of iterations required to reach specific Dice Scores across interactive models. Models that failed to reach the target Dice Score within six iterations are assigned an iteration count of ten. Failure rate is provided in the appendix. SPA consistently achieves lower failure rates and requires fewer iterations.

4.3.2. Efficiency Analysis on Different Interactive Models

We conducted an efficiency analysis to quantify the number of iterations required to reach specific Dice Scores, with a maximum of six iterations. Models that failed to reach the target Dice Score within the limit were assigned an iteration count of ten. The failure rate is provided in the appendix. Our proposed method, SPA, consistently has lower failure rates and requires fewer iterations to achieve superior segmentation performance compared to other models.

SPA outperforms all other interactive models in terms of interaction efficiency, as shown in Fig. 4. On the REFUGE2 dataset, it requires fewer than five iterations to achieve a Dice Score of 87%, whereas SAM-U V2 needs

5.6 iterations to reach a Dice Score of just 84%. In the LIDC dataset, SPA achieves 75% Dice Score with only 2.7 iterations on average, while other models typically require four or more iterations. Similarly, on the Kidney dataset, SPA reaches a Dice Score of 92% with 3.2 iterations, while other SAM-series models often need four to ten iterations. Notably, SPA reaches a Dice Score of 95% within eight iterations, but other models struggle to converge within the ten-iteration limit.

SPA shows generalization and robustness to unseen preferences. To show this, we conducted a leave-one-user-out experiment three times, each time leaving a different user out during the training phase. The reported results are averaged

Table 2. SPA Demonstrates Strong Prediction Alignment with Individual Users. Alignment analysis by Dice Score (%) on the REFUGE2 optic cup segmentation task. The ground truth combines annotations from Clinicians 2, 4, 5, 6, and 7, excluding Clinicians 1 and 3. Predictions are compared with individual clinicians (columns) across interaction iterations (rows). The predictions show increasing alignment with included clinicians and divergence from excluded clinicians.

| Iteration | Clinician 1 | Clinician 2 | Clinician 3 | Clinician 4 | Clinician 5 | Clinician 6 | Clinician 7 |
|-----------|-----------------------|-----------------------|-----------------------|-----------------------|-----------------------|-----------------------|-----------------------|
| 1 | 75.02 | 78.92 | 83.98 | 78.25 | 80.81 | 84.86 | 59.35 |
| 2 | 74.03 (-1.32%) | 80.58 (+2.10%) | 84.03 (+0.05%) | 78.88 (+0.81%) | 81.92 (+1.37%) | 85.62 (+0.90%) | 60.43 (+1.82%) |
| 3 | 73.61 (-1.88%) | 80.88 (+2.48%) | 83.68 (-0.36%) | 79.16 (+1.16%) | 82.17 (+1.68%) | 85.87 (+1.19%) | 60.79 (+2.43%) |
| 4 | 73.35 (-2.23%) | 81.29 (+3.00%) | 83.40 (-0.69%) | 79.19 (+1.20%) | 82.32 (+1.87%) | 86.06 (+1.41%) | 61.06 (+2.88%) |
| 5 | 73.27 (-2.33%) | 81.35 (+3.08%) | 83.32 (-0.79%) | 79.17 (+1.18%) | 82.48 (+2.07%) | 85.90 (+1.23%) | 61.14 (+3.02%) |
| 6 | 73.15 (-2.49%) | 81.54 (+3.32%) | 83.30 (-0.81%) | 79.23 (+1.25%) | 82.65 (+2.28%) | 86.03 (+1.38%) | 61.34 (+3.35%) |

across these three runs, while individual user statistics are provided in the appendix. On REFUGE2 optic cup segmentation task, SPA achieves a 75% Dice Score in an average of 3.01 iterations, whereas other models require more than 3.6 iterations to reach similar accuracy. For a Dice Score of 84%, SPA requires an average of 5.02 iterations, surpassing the second-best model, MedSAM, by 0.94 iterations. In addition, SPA is transferable between images for the same user. The Dice Score improves from 91.68% to 92.43% on Kidney dataset by using user-adapted GMM parameters.

SPA’s improved efficiency is further substantiated with a human user study. We invited five medical professionals, each with over five years of graduate-level expertise, to annotate 100 fundus images from the REFUGE2 dataset. Across all annotators, SPA consistently required fewer interactions and less time compared to MedSAM. For example, one individual required an average of 6.62 seconds and 4.33 iterations per image with MedSAM, but only 4.34 seconds and 2.46 iterations with SPA. Another annotator took 7.40 seconds and 5.60 iterations per image with MedSAM, but just 4.77 seconds and 3.58 iterations with SPA. Similarly, for the remaining annotators, SPA required an average of 4.56, 5.03, and 4.82 seconds per image, compared to 6.91, 8.04, and 7.60 seconds with MedSAM. This significant reduction in both time and interactions highlights SPA’s superior efficiency. User study details are provided in the appendix.

4.3.3. Prediction Alignment with Clinician Feedback in Model Adaptation

Table 2 shows prediction alignment results for optic cup segmentation on the REFUGE2 dataset, comparing SPA’s predictions with individual clinicians’ annotations after each iteration. In this case, the ground truth is defined as the weighted average of annotations from Clinicians 2, 4, 5, 6, and 7, excluding Clinicians 1 and 3. After each interaction, the Dice Scores for the included clinicians consistently improve, indicating that SPA is adapting to the desired context. For example, Clinician 2’s score increases from 78.92% to 81.54% (+3.32%), with similar positive trends for Clinicians 4, 5, 6, and 7 (+ 1.25%, +2.28%, +1.38%, and +3.35%, respectively). In contrast, the Dice Scores for the excluded clinicians, such as Clinicians 1 and 3, show a consistent

decline (-2.49% and -0.81%), indicating that the model is effectively excluding irrelevant clinicians. This multi-choice-based refinement demonstrates SPA’s ability to align predictions with the included clinicians while excluding those not part of the ground truth. Visualization of this alignment is provided in the appendix.

4.3.4. Ablation Study

In this section, we conducted an ablation study on key components of SPA, including random sampling from the preference distribution (Random Gaussian), updating the mean and variance (Gaussian), and adjusting distribution weights (Mixture Gaussian). Table 3 shows the ablation results, with segmentation performance evaluated by Dice Score on the REFUGE2 and Kidney datasets after three iterations.

When only randomly sampling is used without calibrating the mean, variance, or weight of the preference distribution, the Dice Scores are 80.29% for REFUGE2 and 90.05% for the Kidney dataset. Training the mean and variance improves the scores to 84.12% and 92.06%, respectively. Additionally, training the distribution weights alone raises the scores to 82.87% for REFUGE2 and 92.29% for Kidney. Finally, combining all three components which results to calibrating distribution mean, variance, and weight to form the preference distribution yields the highest performance, with Dice Scores of 85.42% for REFUGE2 and 94.26% for the Kidney dataset. This highlights the complementary benefits of each component in achieving optimal segmentation performance.

Table 3. Effectiveness of Network Modules in SPA. Ablation study evaluating the impact of network components on segmentation performance for the REFUGE2 and Kidney datasets after three iterations. The table compares random sampling (Random Gaussian), updating the mean and variance (Gaussian), and updating distribution weights (Mixture Gaussian). Combining all modules achieves the highest Dice Scores, highlighting their complementary benefits in optimizing segmentation performance.

| Random Gaussian | Gaussian | Mixture Gaussian | REFUGE2 | Kidney |
|-----------------|----------|------------------|--------------|--------------|
| ✓ | | | 80.29 | 90.05 |
| ✓ | ✓ | | 84.12 | 92.06 |
| ✓ | | ✓ | 82.87 | 92.29 |
| ✓ | ✓ | ✓ | 85.42 | 94.26 |

5. Conclusion

In this work, we introduce SPA, a novel segmentation framework that efficiently adapts to user preferences with minimal human effort. By offering users multi-choice options based on image uncertainties at interactions, SPA reduces user workload and ensures preference-specific predictions. The proposed preference distribution allows the model to dynamically adapt to user feedback during inference, accelerating convergence and enhancing interaction efficiency. Reported experiments show that SPA outperforms deterministic, uncertainty-aware, and interactive SOTA models, demonstrating strong adaptability in different clinical contexts while requiring significantly less time and effort. These results highlight SPA’s potential to contribute to improving clinical workflows in real-world medical applications.

Acknowledgement

Jiayuan Zhu is supported by the Engineering and Physical Sciences Research Council (EPSRC) under grant EP/S024093/1 and Global Health R&D of Merck Healthcare, Ares Trading S.A. (an affiliate of Merck KGaA, Darmstadt, Germany), Eysins, Switzerland (Crossref Funder ID: 10.13039/100009945). Junde Wu is supported by the Engineering and Physical Sciences Research Council (EPSRC) under grant EP/S024093/1 and GE HealthCare.

References

- [1] Samuel G. Armato, Geoffrey McLennan, Luc Bidaut, Michael F. McNitt-Gray, Charles R. Meyer, Anthony P. Reeves, Binsheng Zhao, Denise R. Aberle, Claudia I. Henschke, Eric A. Hoffman, Ella A. Kazerooni, Heber MacMahon, Edwin J. R. van Beek, David Yankelevitz, Alberto M. Biancardi, Peyton H. Bland, Matthew S. Brown, Roger M. Engelmann, Gary E. Laderach, Daniel Max, Richard C. Pais, David P.-Y. Qing, Rachael Y. Roberts, Amanda R. Smith, Adam Starkey, Poonam Batra, Philip Caligiuri, Ali Farooqi, Gregory W. Gladish, C. Matilda Jude, Reginald F. Munden, Iva Petkovska, Leslie E. Quint, Lawrence H. Schwartz, Baskaran Sundaram, Lori E. Dodd, Charles Fenimore, David Gur, Nicholas Petrick, John Freymann, Justin Kirby, Brian Hughes, Alessi Vande Castele, Sangeeta Gupte, Maha Sallam, Michael D. Heath, Michael H. Kuhn, Ekta Dharaiya, Richard Burns, David S. Fryd, Marcos Salganicoff, Vikram Anand, Uri Shreter, Stephen Vastagh, Barbara Y. Croft, and Laurence P. Clarke. The Lung Image Database Consortium (LIDC) and Image Database Resource Initiative (IDRI): A Completed Reference Database of Lung Nodules on CT Scans. *Medical Physics*, 38(2):915–931, 2011. [6](#)
- [2] Byron Ballou, Gregory W. Fisher, Thomas R. Hakala, and Daniel L. Farkas. Tumor Detection and Visualization Using Cyanine Fluorochrome-Labeled Antibodies. *Biotechnology Progress*, 13(5):649–658, 1997. [_eprint:](#) <https://onlinelibrary.wiley.com/doi/pdf/10.1021/bp970088t>. [1](#)
- [3] Christian F. Baumgartner, Kerem C. Tezcan, Krishna Chaitanya, Andreas M. Hötker, Urs J. Muehlematter, Khoshy Schawkat, Anton S. Becker, Olivio Donati, and Ender Konukoglu. PHISeg: Capturing Uncertainty in Medical Image Segmentation. In *Medical Image Computing and Computer Assisted Intervention – MICCAI 2019*, pages 119–127, Cham, 2019. Springer International Publishing. [1, 2](#)
- [4] Hu Cao, Yueyue Wang, Joy Chen, Dongsheng Jiang, Xiaopeng Zhang, Qi Tian, and Manning Wang. Swin-Unet: Unet-like Pure Transformer for Medical Image Segmentation, 2021. arXiv:2105.05537 [cs, eess]. [6](#)
- [5] Jieneng Chen, Yongyi Lu, Qihang Yu, Xiangde Luo, Ehsan Adeli, Yan Wang, Le Lu, Alan L. Yuille, and Yuyin Zhou. TransUNet: Transformers Make Strong Encoders for Medical Image Segmentation, 2021. arXiv:2102.04306 [cs]. [1, 6](#)
- [6] Xi Chen, Zhiyan Zhao, Yilei Zhang, Manni Duan, Donglian Qi, and Hengshuang Zhao. FocalClick: Towards Practical Interactive Image Segmentation, 2022. arXiv:2204.02574 [cs]. [1](#)
- [7] Kenneth Clark, Bruce Vendt, Kirk Smith, John Freymann, Justin Kirby, Paul Koppel, Stephen Moore, Stanley Phillips, David Maffitt, Michael Pringle, Lawrence Tarbox, and Fred Prior. The Cancer Imaging Archive (TCIA): Maintaining and Operating a Public Information Repository. *Journal of Digital Imaging*, 26(6):1045–1057, 2013. [6](#)
- [8] Guoyao Deng, Ke Zou, Kai Ren, Meng Wang, Xuedong Yuan, Sancong Ying, and Huazhu Fu. SAM-U: Multi-box prompts triggered uncertainty estimation for reliable SAM in medical image, 2023. arXiv:2307.04973 [cs]. [3, 6](#)
- [9] Huihui Fang, Fei Li, Junde Wu, Huazhu Fu, Xu Sun, Jaemin Son, Shuang Yu, Menglu Zhang, Chenglang Yuan, Cheng Bian, Baiying Lei, Benjian Zhao, Xinxing Xu, Shaohua Li, Francisco Fumero, José Sigut, Haidar Almubarak, Yakoub Bazi, Yuanhao Guo, Yating Zhou, Ujjwal Baid, Shubham Innani, Tianjiao Guo, Jie Yang, José Ignacio Orlando, Hrvoje Bogunović, Xiulan Zhang, and Yanwu Xu. REFUGE2 Challenge: A Treasure Trove for Multi-Dimension Analysis and Evaluation in Glaucoma Screening, 2022. arXiv:2202.08994 [cs, eess]. [5](#)
- [10] Melody Y. Guan, Varun Gulshan, Andrew M. Dai, and Geoffrey E. Hinton. Who Said What: Modeling Individual Labelers Improves Classification, 2018. arXiv:1703.08774 [cs]. [2, 6](#)
- [11] Kaiming He, Xinlei Chen, Saining Xie, Yanghao Li, Piotr Dollár, and Ross Girshick. Masked Autoencoders Are Scalable Vision Learners, 2021. arXiv:2111.06377 [cs]. [4](#)
- [12] Mohammad Hesam Hesamian, Wenjing Jia, Xiangjian He, and Paul Kennedy. Deep Learning Techniques for Medical Image Segmentation: Achievements and Challenges. *Journal of Digital Imaging*, 32(4):582–596, 2019. [1](#)
- [13] Ling Huang, Su Ruan, Yucheng Xing, and Mengling Feng. A review of uncertainty quantification in medical image analysis: Probabilistic and non-probabilistic methods. *Medical Image Analysis*, 97:103223, 2024. [2](#)
- [14] Martin Holm Jensen, Dan Richter Jørgensen, Raluca Jalaboi, Mads Eiler Hansen, and Martin Aastrup Olsen. Improving Uncertainty Estimation in Convolutional Neural Networks

- Using Inter-rater Agreement. In *Medical Image Computing and Computer Assisted Intervention – MICCAI 2019*, pages 540–548, Cham, 2019. Springer International Publishing. 2, 6
- [15] Wei Ji, Shuang Yu, Junde Wu, Kai Ma, Cheng Bian, Qi Bi, Jingjing Li, Hanruo Liu, Li Cheng, and Yefeng Zheng. Learning Calibrated Medical Image Segmentation via Multi-rater Agreement Modeling. In *2021 IEEE/CVF Conference on Computer Vision and Pattern Recognition (CVPR)*, pages 12336–12346, 2021. ISSN: 2575-7075. 2, 4, 6
- [16] Alex Kendall and Yarin Gal. What Uncertainties Do We Need in Bayesian Deep Learning for Computer Vision?, 2017. arXiv:1703.04977 [cs]. 1
- [17] Alexander Kirillov, Eric Mintun, Nikhila Ravi, Hanzi Mao, Chloe Rolland, Laura Gustafson, Tete Xiao, Spencer Whitehead, Alexander C. Berg, Wan-Yen Lo, Piotr Dollár, and Ross Girshick. Segment Anything, 2023. arXiv:2304.02643 [cs]. 1, 3, 4, 6
- [18] Armen Der Kiureghian and Ove Ditlevsen. Aleatory or epistemic? Does it matter? *Structural Safety*, 31(2):105–112, 2009. 2
- [19] Simon A. A. Kohl, Bernardino Romera-Paredes, Clemens Meyer, Jeffrey De Fauw, Joseph R. Ledsam, Klaus H. Maier-Hein, S. M. Ali Eslami, Danilo Jimenez Rezende, and Olaf Ronneberger. A Probabilistic U-Net for Segmentation of Ambiguous Images, 2018. 2, 6
- [20] Simon A. A. Kohl, Bernardino Romera-Paredes, Klaus H. Maier-Hein, Danilo Jimenez Rezende, S. M. Ali Eslami, Pushmeet Kohli, Andrew Zisserman, and Olaf Ronneberger. A Hierarchical Probabilistic U-Net for Modeling Multi-Scale Ambiguities, 2019. arXiv:1905.13077 [cs]. 6
- [21] Simon A. A. Kohl, Bernardino Romera-Paredes, Clemens Meyer, Jeffrey De Fauw, Joseph R. Ledsam, Klaus H. Maier-Hein, S. M. Ali Eslami, Danilo Jimenez Rezende, and Olaf Ronneberger. A Probabilistic U-Net for Segmentation of Ambiguous Images, 2019. arXiv:1806.05034 [cs, stat]. 1
- [22] Hongwei Bran Li, Fernando Navarro, Ivan Ezhov, Amirhossein Bayat, Dhritiman Das, Florian Kofler, Suprosanna Shit, Diana Waldmannstetter, Johannes C. Paetzold, Xiaobin Hu, Benedikt Wiestler, Lucas Zimmer, Tamaz Amiranashvili, Chinmay Prabhakar, Christoph Berger, Jonas Weidner, Michelle Alonso-Basant, Arif Rashid, Ujjwal Baid, Wesam Adel, Deniz Ali, Bhakti Baheti, Yingbin Bai, Ishaan Bhatt, Sabri Can Cetindag, Wenting Chen, Li Cheng, Prasad Dutand, Lara Dular, Mustafa A. Elattar, Ming Feng, Shengbo Gao, Henkjan Huisman, Weifeng Hu, Shubham Innani, Wei Jiat, Davood Karimi, Hugo J. Kuijf, Jin Tae Kwak, Hoang Long Le, Xiang Lia, Huiyan Lin, Tongliang Liu, Jun Ma, Kai Ma, Ting Ma, Ilkay Oksuz, Robbie Holland, Arlindo L. Oliveira, Jimut Bahan Pal, Xuan Pei, Maoying Qiao, Anindo Saha, Raghavendra Selvan, Linlin Shen, Joao Lourenco Silva, Ziga Spiclin, Sanjay Talbar, Dadong Wang, Wei Wang, Xiong Wang, Yin Wang, Ruiling Xia, Kele Xu, Yanwu Yan, Mert Yergin, Shuang Yu, Lingxi Zeng, YingLin Zhang, Jiachen Zhao, Yefeng Zheng, Martin Zukovec, Richard Do, Anton Becker, Amber Simpson, Endre Konukoglu, Andras Jakab, Spyridon Bakas, Leo Joskowicz, and Bjoern Menze. QUBIQ: Uncertainty Quantification for Biomedical Image Segmentation Challenge, 2024. arXiv:2405.18435 [cs, eess]. 6
- [23] Qin Liu, Zhenlin Xu, Gedas Bertasius, and Marc Niethammer. SimpleClick: Interactive Image Segmentation with Simple Vision Transformers, 2023. arXiv:2210.11006 [cs]. 1
- [24] Jun Ma, Yuting He, Feifei Li, Lin Han, Chenyu You, and Bo Wang. Segment Anything in Medical Images. *Nature Communications*, 15(1):654, 2024. arXiv:2304.12306 [cs, eess]. 3, 6
- [25] Pataje G.S. Prasanna, Helen B. Stone, Rosemary S. Wong, Jacek Capala, Eric J. Bernhard, Bhadrasain Vikram, and C. N. Coleman. Normal tissue protection for improving radiotherapy: Where are the Gaps? *Translational cancer research*, 1(1):35–48, 2012. 1
- [26] Olaf Ronneberger, Philipp Fischer, and Thomas Brox. U-Net: Convolutional Networks for Biomedical Image Segmentation, 2015. arXiv:1505.04597 [cs]. 1, 6
- [27] Christian Rupprecht, Iro Laina, Robert DiPietro, Maximilian Baust, Federico Tombari, Nassir Navab, and Gregory D. Hager. Learning in an Uncertain World: Representing Ambiguity Through Multiple Hypotheses, 2017. arXiv:1612.00197 [cs]. 1
- [28] Tomas Sakanis, Fausto Milletari, Holger Roth, Panagiotis Korfiatis, Petro Kostandy, Kenneth Philbrick, Zeynettin Akkus, Ziyue Xu, Daguang Xu, and Bradley J. Erickson. Interactive segmentation of medical images through fully convolutional neural networks, 2019. arXiv:1903.08205 [cs]. 3
- [29] Konstantin Sofiiuk, Ilia A. Petrov, and Anton Konushin. Reviving Iterative Training with Mask Guidance for Interactive Segmentation, 2021. arXiv:2102.06583 [cs]. 1
- [30] Nima Tajbakhsh, Jae Y. Shin, Suryakanth R. Gurudu, R. Todd Hurst, Christopher B. Kendall, Michael B. Gotway, and Jianming Liang. Convolutional Neural Networks for Medical Image Analysis: Full Training or Fine Tuning? *IEEE Transactions on Medical Imaging*, 35(5):1299–1312, 2016. arXiv:1706.00712 [cs]. 1
- [31] Guotai Wang, Wenqi Li, Maria A. Zuluaga, Rosalind Pratt, Premal A. Patel, Michael Aertsen, Tom Doel, Anna L. David, Jan Deprest, Sebastien Ourselin, and Tom Vercauteren. Interactive Medical Image Segmentation using Deep Learning with Image-specific Fine-tuning. *IEEE Transactions on Medical Imaging*, 37(7):1562–1573, 2018. arXiv:1710.04043 [cs]. 3
- [32] Junde Wu, Wei Ji, Yuanpei Liu, Huazhu Fu, Min Xu, Yanwu Xu, and Yueming Jin. Medical SAM Adapter: Adapting Segment Anything Model for Medical Image Segmentation, 2023. arXiv:2304.12620 [cs]. 3, 6
- [33] Le Zhang, Ryutaro Tanno, Mou-Cheng Xu, Chen Jin, Joseph Jacob, Olga Ciccarelli, Frederik Barkhof, and Daniel C. Alexander. Disentangling Human Error from the Ground Truth in Segmentation of Medical Images, 2020. arXiv:2007.15963 [cs]. 2
- [34] Jiayuan Zhu, Yunli Qi, and Junde Wu. Medical SAM 2: Segment medical images as video via Segment Anything Model 2, 2024. arXiv:2408.00874 [cs]. 3
- [35] Ke Zou, Zhihao Chen, Xuedong Yuan, Xiaojing Shen, Meng Wang, and Huazhu Fu. A Review of Uncertainty

Estimation and its Application in Medical Imaging, 2023.
arXiv:2302.08119 [cs, eess]. [2](#)